Aeroacoustics Conferences
June 14-17, 2022, Southampton, UK
28th AIAA/CEAS Aeroacoustics 2022 Conference

10.2514/6.2022-2957

Interferometric Rayleigh Scattering for flow analysis : Fabry-Pérot interferogram analysis

Igor Kurek*,Pierre Lecomte †,Thomas Castelain ‡,Emmanuel Jondeau§,Christophe Bailly¶

A post processing routine is developed to analyse interferograms provided by Rayleigh scattering measurements whose aim is to locally estimate the velocity and temperature of a free flow. Its precision is assessed on synthetic interferograms, both for the interferometer transfer function and for Rayleigh interferograms. The algorithm succeed to give proper estimation of the interferometer transfer function parameters, within 1% error, as well for the velocity and temperature. The precision of the latter is assessed with interferograms with added background noise to simulate experimental interferograms.

I. Nomenclature

c	=	speed of light in the vacuum (m.s^{-1})
d	=	distance between the reflective surfaces (m)
f_c	=	collimating lens focal length (m)
f_f	=	fringe forming lens focal distance (m)
FWMW	=	Full Width at Half Maximum
h	=	vertical origin of the laser (m)
I_b	=	noise intensity
I_0	=	incident light intensity
I_R	=	scattered light intensity
k	=	order of the first fringe
k_b	=	Boltzmann constant (J.K^{-1})
κ	=	thermal conductivity (W.m^{-1}.K^{-1})
$\vec{k_0}$	=	wave vector of the incident light (m^{-1})
$\vec{k_s}$	=	wave vector of the scattered light (m^{-1})
$\vec{K}$	=	interaction vector (m^{-1})
l_n	=	mean free path of the molecules (m)
L	=	laser shape function
n	=	order number
$\mathcal{N}$	=	number density (m^{-3})
N_E	=	effective finesse
N_R	=	reflective finesse
m	=	mass of single molecule (kg)
r	=	distance to the center of the interferogram (m)
r_N	=	radius of the Nth fringe (m)
R	=	reflectivity of the mirrors
S_R	=	spectrum of the scattered light
T	=	temperature (K)

*PhD Student, Univ Lyon, Ecole Centrale de Lyon, CNRS, INSA Lyon, Univ Claude Bernard Lyon I, LMFA, UMR5509, 69130, Ecully, France, igor.kurek@ec-lyon.fr

†Assistant Professor, Univ Lyon, Ecole Centrale de Lyon, CNRS, INSA Lyon, Univ Claude Bernard Lyon I, LMFA, UMR5509, 69130, Ecully, France, pierre.lecomte@univ-yon1.fr

‡Assistant Professor, Univ Lyon, Ecole Centrale de Lyon, CNRS, INSA Lyon, Univ Claude Bernard Lyon I, LMFA, UMR5509, 69130, Ecully, France, thomas.castelain@ec-lyon.fr

§Research Engineer, Univ Lyon, Ecole Centrale de Lyon, CNRS, INSA Lyon, Univ Claude Bernard Lyon I, LMFA, UMR5509, 69130, Ecully, France, emmanuel.jondeau@ec-lyon.fr

¶Professor, Univ Lyon, Ecole Centrale de Lyon, CNRS, INSA Lyon, Univ Claude Bernard Lyon I, LMFA, UMR5509, 69130, Ecully, France, christophe.bailly@ec-lyon.fr, senior member

u	=	velocity (m.s^{-1})
u_0	=	velocity related to thermal effect (m.s^{-1})
V_s	=	sample volume
x	=	dimentionless frequency
(X, Y)	=	Cartesian coordinate of the interferogram (m)
(X_c, Y_c)	=	coordinate of the interferogram center (m)
y	=	Rayleigh scattering model parameter
ρ	=	density (kg.m^{-3})
φ	=	phase shift
φ_0	=	phase shift at the pattern centre
Φ_0	=	rest of the phase shift at the centre
γ	=	ratio of heat capacity
η	=	shear viscosity (Pa.s)
η_b	=	bulk viscosity (Pa.s)
θ	=	angle of the incident light
μ	=	refractive index
χ_s	=	scattering angle
λ	=	wavelength in the vacuum (m)
λ_0	=	wavelenght of the incident light (m)
λ_s	=	wavelenght of the scattered light (m)
λ_i	=	interaction wavelength (m)
σ	=	FMHM of the laser shape function
ν	=	frequency of the light (Hz)
ν_s	=	frequency of the scattered light (Hz)
Δ	=	difference between the internal and external radii of the last annulus (m)
$\Delta\nu_T$	=	spectrum broadening due to temperature (Hz)
$\Delta\nu$	=	frequency shift due to bulk velocity (Hz)

II. Introduction

There is a continuous interest in aeroacoustics for the development and application of advanced optical methods to non-intrusively characterize both the velocity and temperature of a flow. Interferometric Rayleigh Scattering (IRS) is a non intrusive and high frequency rate experimental technique that meets its challenges. IRS is one such method that allows for time-resolved measurements in fluid mechanics. The underlying physical process is that molecules submitted to an electromagnetic field such as light are excited and become secondary sources by scattering a part of this light. In a laboratory context, the primary light source can be a continuous wave (CW) [1–6] or a pulsed [7–9] laser. If the gas composition is constant, the total intensity of the Rayleigh scattered light is directly proportional to the gas density ρ. In a given volume control, as the number of scattering molecules increases, and consequently the density, the total scattered light increases proportionally. Therefore, the light intensity information can be used to determine the flow density. Moreover, in low speeds flows where the pressure fluctuations can be neglected with regards to the temperature and density fluctuations, the density information can also be used to retrieve the temperature fluctuations [10].
The spectral content of the scattered light provides information on bulk velocity and temperature of molecules in a given volume. The shift in frequency between the laser incident light and the Rayleigh scattered light is proportional to the bulk flow velocity u and the width of the spectral content of Rayleigh scattered light is related to the gas temperature T. Simultaneous and time resolved measurement of temperature, velocity and density [1, 2, 11] is then achieved.

The spectrum of the Rayleigh scattered light is retrieved by using a Fabry-Perot interferometer. The latter produces an inteferogram in a shape of concentrinc rings. This work aims to develop and test a routine to analyse these interferograms. The method is inspired by the annular summing technique [12], adapted for IRS measurements. A parametric study is made on synthetic interferograms to test the robustness of the method. The final aim of this contribution is to assess the uncertainty of real measurements for flow temperature and velocity due to the interferogram analysis process by itself.

III. Interferometric Rayleigh scattering

A. Rayleigh scattering

Rayleigh scattering describes as an elastic phenomenon, meaning that it does not change the internal energy of the molecule scattering the incident light [13]. Frequency shifts arise from translational motion of the molecules inducing a Doppler effect. The spectrum of the scattered light and its differences relatively to the spectral content of the incident light is representative of the molecules motion. In this work, the independent main sources of motion are thermal agitation and bulk velocity of the molecules, as the media is non reactive.

Considering $\vec{k_0}$ the wave vector of the incident light emitted by the laser, $\vec{k_s}$ is the wave vector of the scattered light in the observation direction, and its wavelength is close to the incident one, $\lambda_0 \simeq \lambda_s$. The scattered light has a broadband spectrum, but each frequency component is analysed separately. The geometry of the scattering problem is shown in Figure 1. The sample volume V_s defines the intersection between the incident light beam and the observation optical axis. The observation angle of the scattering is noted χ_s.

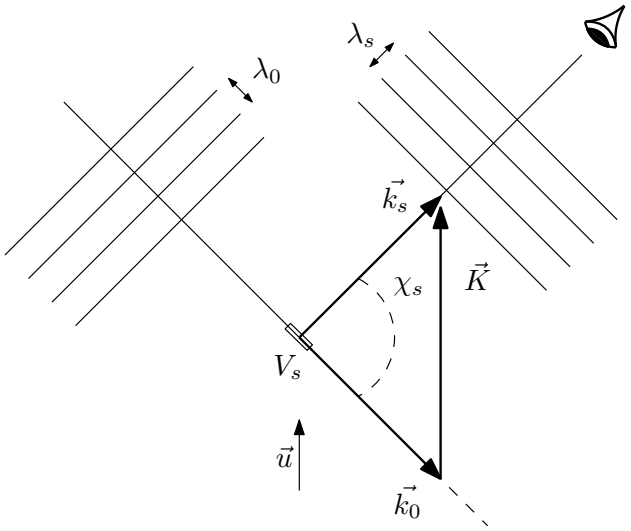

Fig. 1 Scattering vector diagram. λ_0 and λ_s are the wavelength of the incident and scattered light respectively, with k_0 and k_s their associated wavenumber. The angle between $\vec{k_0}$ and $\vec{k_s}$ is noted χ_s, $\vec{u}$ and $\vec{K}$ are the velocity and interaction vector.

$\vec{K}$ is the interaction vector and is the bisector of the incident and scattered light wave vector. It is equal to:

$$\vec{K} = \vec{k_s} - \vec{k_0} \tag{1}$$

and its norm K is given by :

$$K = |\vec{K}| = \frac{4\pi}{\lambda_0} \sin(\chi_s/2) \tag{2}$$

while $\lambda_i = [\lambda_0/2 \sin(\chi_s/2)]$ is the associated wavelength, referred to as the interaction wavelength.

1. Temperature effects

The effect of temperature on the shape of the scattered light spectrum strongly depends on the gas regime, in the sense of the gas kinetic theory. These regimes are distinguished depending on the value of the parameter y, which corresponds to the ratio between the interaction wavelength λ_i to the mean free path l_n of the molecules and is therefore the inverse of the Knudsen number. The y parameter is used in most models to predict the shape of the scattered light spectrum according to certain flow parameters, as the Tenti S6 model [14]. It is known to be the more precise, with only 2% error on the spectrum in air [15]. This parameter can be expressed as:

$$y = \frac{\mathcal{N} k_B T}{\sqrt{2} K u_0 \eta} \tag{3}$$

The velocity $u_0 = \sqrt{k_B T/m}$ is related to the thermal effect, where m is the mass of the molecule, $\mathcal{N}$ is the number density and k_B the Boltzmann constant. η is the shear viscosity of the gas, whose temperature dependence is expressed with the Sutherland formula [13]:

$$\eta = \eta_0 \left(\frac{T}{T_0}\right)^{3/2} \left(\frac{T_0 + S}{T + S}\right) \tag{4}$$

with $\eta_0 = 1.716.10^{-5}$ N.s.m^{-2}, $T_0 = 273$ K and $S = 111$K. An example of spectral lineshapes in the different regimes (y=0.59, y=0.80, y=1.15) is shown in Figure 2, calculated with the S6 model at atmospheric pressure.

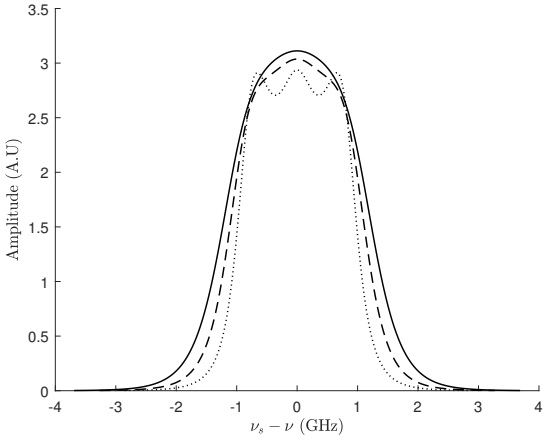

Fig. 2 Spectral lineshape centred on the laser frequency of Rayleigh scattering in air at atmospheric pressure, calculated with the S6 model. — T=373 K (y=0,59), - - - T=293 K (y=0,80), ... T=223 K (y=1.15)

The first regime is called Knudsen regime, or collisionless regime. The mean free path of molecules is larger than the interaction wavelength, therefore $y < 1$. It corresponds to low density or high temperature. In this regime, the uncorrelated thermal motion of molecules provides a spectrum which has a symmetrical Gaussian shape. This is called the thermally broadened Rayleigh line. The scattering reflects the motion of the molecules.

For a gas at an absolute temperature T in the Knudsen regime, the expression for the spectrum broadening due to temperature is given by Miles [13]:

$$\Delta\nu_T = \frac{K}{2\pi}\sqrt{\frac{8 k_B T \ln(2)}{m}} \tag{5}$$

where $\Delta\nu_T$ is the Full Width at Half Maximum (FWHM) of the Gaussian line shape.

The second regime corresponds to the kinetic regime associated with high pressure or low temperature. A shorter mean free path is expected, which thus become of the same order as the interaction wavelength. This means that y is close to unity. In this regime, density fluctuations begin to contribute to the spectral shape. The origin of these density fluctuations are generally acoustic waves that travels at the speed of sound. This makes appear side bands, named Brillouin-Mandel'shtan scattering lines. These are sharply peaked in high pressure media. In this work, and in most aerodynamic applications the gas regime fells into the kinetic regime [1, 16]. This justifies the uses of a scattering model which can transcribe the features of the spectral shape.

The third and last regime starts when the interference length λ_i is greater than the mean free path. In these conditions the gas is at the hydrodynamic regime, and y is greater than unity. In this regime, the spectrum of the scattered light is

composed of three peaks having a lorentzian shape. The acoustic sidebands are located at the frequency shift associated with the speed of sound in the media. Since the speed of sound is related to the temperature, these sidebands can be used to determine the temperature in the flow. The central peak is associated with the thermal diffusion rate. The central peak is also of importance, since the ratio of the total central peak intensity to the total sidebands intensity, for a single component gas, is $\gamma - 1$, γ being the specific heat ratio.

In such models, the frequency of the scattered light ν_s is usually normalised in units of x, defined as:

$$x = \frac{2\pi(\nu_s - \nu)}{\sqrt{2}Ku_0} \tag{6}$$

which is centred at the frequency of the incident light ν. This is convenient because it permits to express the frequency with regards to their shift compared to the incident light frequency ν and not in absolute frequency, which are usually very high. With this formulation, x takes a zero value for a frequency ν_s equal to the frequency of the incident light. Moreover, the spectrum of the scattered light S_R is only a function of these two parameters x and y.
The S6 model consider gas as a single species and with spherical particles. Its inputs are the properties of the gas, such as the shear viscosity η the bulk viscosity η_b and the thermal conductivity κ. These can be those of pure nitrogen [1], even though oxygen and other gases are also present in air. However air can be considered as an effective single-component gas with temperature-scaled values for the relevant macroscopic transport coefficients [15]. That is the approach followed here. For a fixed gas composition, the spectral shape of the scattered light only depends on the temperature T.

2. Flow velocity effects

In addition to small-scale motion related to temperature effects, there may be particular motion related to convection, as in the case of a gas flowing with velocity $\vec{u}$. From the point of view of the scattered light spectrum, molecular convection results in a frequency shift of the entire spectrum. This $\Delta\nu$ offset is expressed by the scalar product:

$$\Delta\nu = \frac{1}{2\pi}\vec{u} \cdot \vec{K} \tag{7}$$

Equivalently, we can define an angle δ between the velocity vector and the interaction vector. The frequency shift can then be recast as:

$$\Delta\nu = \frac{2u}{\lambda}\cos(\delta)\sin(\chi_s/2) \tag{8}$$

By imposing χ_s =90° and $\vec{K}$ collinear with $\vec{u}$ such as represented Figure 1, the previous relationship becomes:

$$\Delta\nu = \frac{\sqrt{2}}{\lambda_0}u \tag{9}$$

The parameter x is redefined to take into account this Doppler shift leading to:

$$x = \frac{2\pi(\nu_s^* - \nu)}{\sqrt{2}Ku_0} \tag{10}$$

where $\nu_s^* = \nu_s + \Delta\nu$. The effect of a Doppler shift on the spectrum induced by a 260 m/s flow velocity is represented on Figure 3. Compared to the spectrum in Figure 2 for the same temperature, the whole spectrum is now shifted in frequency of $\Delta\nu$. These principles apply to any particle in the flow that scatters light, such as undesirable dust.

Velocity effects can also have an impact on the Rayleigh spectral shape. Indeed, turbulent velocity fluctuations can alter the spectrum, and wash out spectral shapes features, such as Brillouin peaks that appears when the scattering angle decreases. However, this effect is negligible for χ_s =90° [17], and is therefore not taken into account in this study.

B. The Fabry-Pérot interferometer

A Fabry-Pérot interferometer is used to decompose the scattered light. An extensive description of the instrument and underlying theory can be found in [18]. The Fabry-Pérot acts as a sharp bandpass filter whose transmittance depends on the wavelength λ of the incident light in the vacuum, the angle θ of the incident light with respect to the optical axis

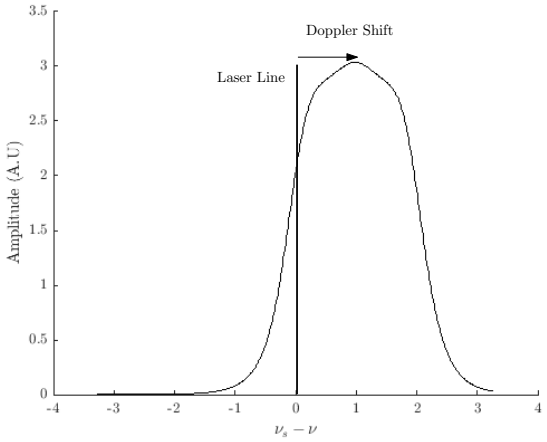

Fig. 3 Rayleigh spectrum calculated with the Tenti S6 model for air at T=293 K at atmospheric pressure. The Doppler shift corresponds to a bulk velocity of 260 m.s^{-1}.

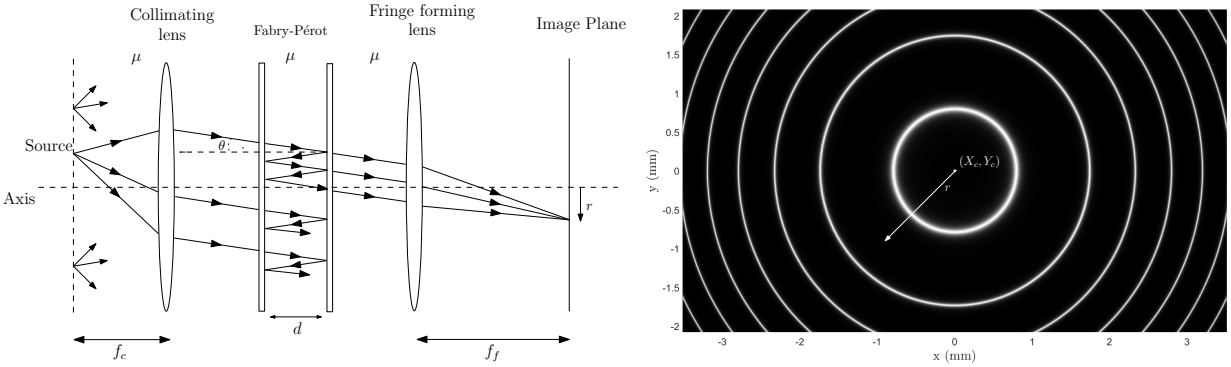

Fig. 4 On the left, a Fabry-Pérot interferometer arrangement with a collimated source. On the right, simulated interferogram: the fringes are formed in the image plane by the fringe forming lens.

inside the cavity, the refractive index μ of the medium separating the two mirrors and the separation d between the surfaces.

We choose an optical assembly represented in Figure 4 including 2 lenses: a collimation lens at the focus of which is the object plane, and a fringe forming lens, of focal length f_f, at the focus of which is placed the image plane. In the object plane there is a light source of wavelength λ. In the same configuration as that represented in Figure 4 but without Fabry-Pérot, it is assumed that the illumination of the image plane is homogeneous, and noted I_0.

For the Fabry-Pérot displayed in Figure 4, and for an incident light beam forming an angle θ with the optical axis, successive reflections on the mirrors of the interferometer induce a path difference between the different rays leaving the interferometer with the same angle θ. The interferogram forming on the image plane is directly conditioned by the phase shift distribution φ in this plane:

$$\varphi = \frac{4\pi\mu d\cos(\theta)}{\lambda} \tag{11}$$

The light intensity distribution in the image plane is given by [18]:

$$I_{\mathrm{FP}}(\varphi) = I_0\left[1 + F\sin^2\left(\frac{\varphi}{2}\right)\right]^{-1} \tag{12}$$

where the term F is defined from the mirror reflectivity R:

$$F = 4R/(1-R)^2 \tag{13}$$

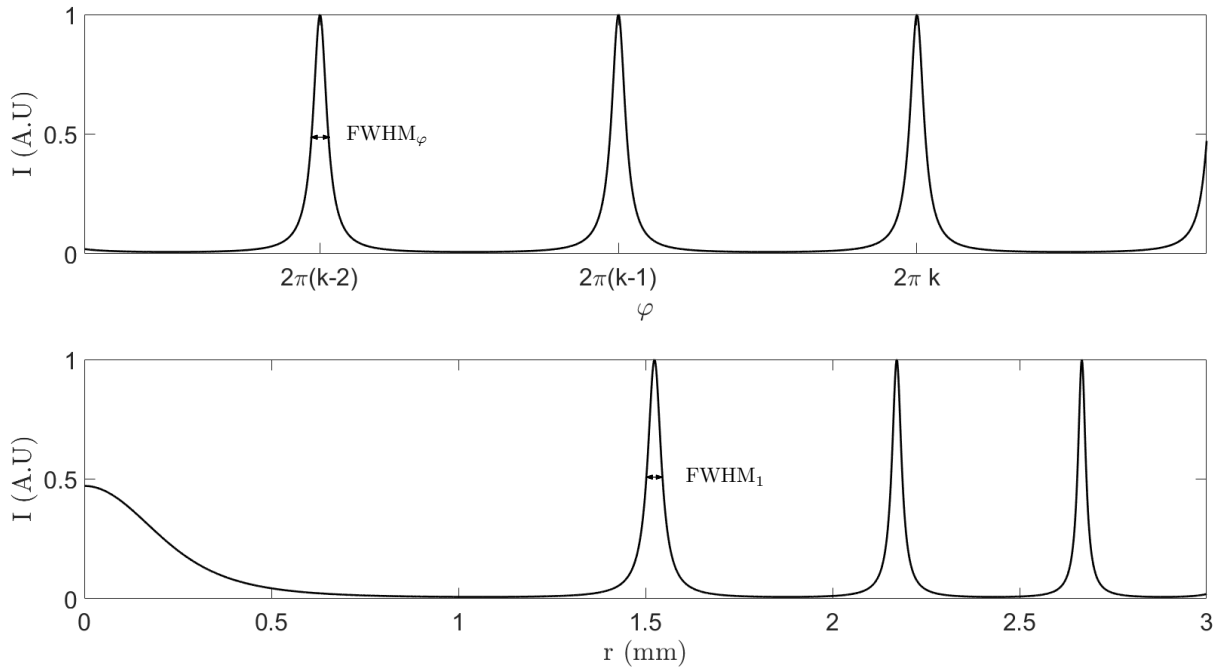

Fig. 5 Top: Intensity distribution in function of the phase shift; bottom: Intensity distribution in function of the radius.

A typical interferogram is shown in Figure 4. The interferogram consists of an ensemble on concentric rings, or fringes. The width of these rings is a characteristic of the device; it is directly linked to F, and is usually expressed using the ideal reflective finesse N_R. In order to introduce this quantity, we use the expression of I_{FP} given by Eq. (12) according to the phase shift φ, plotted in Figure 5. In such a distribution, maxima arise for $\varphi = 2\pi n$ where n is an integer corresponding to the order number. The phase shift φ between successive orders *i.e* between two maxima in this plot, is 2π. The ideal reflective finesse N_R corresponds to the ratio between this interval for φ and the interval corresponding to the *Full-Width at Half-Maximum*, noted FWHM_φ of a peak:

$$N_R = \frac{2\pi}{\text{FWHM}_\varphi} \tag{14}$$

Expressing FWHM_φ from Eq.(12), we obtain for N_R:

$$N_R = \frac{\pi\sqrt{F}}{2} \tag{15}$$

Moreover, the phase shift φ_0 at the center of the interferogram, that is for $\theta = 0$, is given by:

$$\varphi_0 = \frac{4\pi\mu d}{\lambda} \tag{16}$$

We can thus express the phase shift φ from φ_0, and using the small angle approximation for θ, the following relation can be derived:

$$\varphi = \varphi_0 \left(1 - \frac{1}{2}\left(\frac{r}{f_f}\right)^2\right) \tag{17}$$

Therefore, only two instrument parameters take part into the expression of I_{FP}: N_R (or equivalently F or R), related to the mirror reflectivity, and φ_0, including every other physical parameters characteristics of the Fabry-Pérot (d, μ) and its using (λ). To determine φ_0, which can vary according to the ambient temperature conditions during its use, we will rely

on the radii r_N of the different rings of the interferogram. Indeed, recalling that rings forms for $\varphi = 2\pi(k - (N-1))$, with k the first ring order, and N the index of the ring, we can introduce Φ_0 defined as the rest modulo 2π of the phase shift at the center, using the first ring's equation:

$$\begin{aligned} \varphi_1 = 2k\pi &= \varphi_0 - \frac{\varphi_0}{2}\left(\frac{r_1}{f_f}\right)^2 \\ \varphi_0 - 2k\pi &= \frac{\varphi_0}{2}\left(\frac{r_1}{f_f}\right)^2 = \Phi_0 \end{aligned} \tag{18}$$

Then, deriving the equation for the N^{th} ring, the relation between the successive radii and Φ_0 is:

$$r_N = r_1\left(\frac{2(N-1)\pi}{\Phi_0} + 1\right)^{1/2} \tag{19}$$

Finally, recalling that in Eq.(12) the term $F\sin^2(\varphi/2)$ is necessarily 1 when $I_{\text{FP}} = I_0/2$, the relation linking the interferometer finesse to the FWHM of the radial intensity distribution $I(r)$ on the first ring , noted FWHM_1 is:

$$N_R = \frac{\pi}{2\sin\left(\frac{\varphi_0}{8}\frac{2r_1\text{FWHM}_1}{f_f^2}\right)} \tag{20}$$

In general, the ideal finesse N_R corresponds to a value which can only be approximated in an experimental context. In practice, a slight angle between the mirrors, a slight misalignment of the optical axis, a focusing error and all the imperfections require defining an effective fineness N_E, found lower than the ideal finesse by a few units.

C. Interferogram analysis

The analysis of the scattered light interferogram consists of a two step process. First, the Fabry-Pérot characteristics need to be modeled. This is done by investigating the response of the instrument to a monochromatic light, namely the laser light. Based on the instrument function parameters determined experimentally, the interferogram obtained from the scattered light is examined.

1. Interferometer transfer function

The interferogram depends on physical parameters related to the Fabry-Pérot that are prone to drift over time or subject to uncertainties. The Fabry-Pérot characteristics are known within a certain error margin, typically 0.01 mm for the spacing d without considering possible tilt. Uncertainties in the phase shift φ due to small error in d, μ or λ can be significant. Moreover, the effective finesse depends on the quality of the components on the optical chain, and the precision in the arrangement on those, typically the distance between the lens L_f and the image plane.

These parameters are involved in the transfer function of the instrument at a given time. The transfer function, which is defined by the two parameters Φ_0 from Eq. (18) and N_R from Eq (20), is determined by analysing the interferogram obtained for a pure monochromatic light referred to as reference interferogram. On an experimental interferogram, background noise I_b has to be taken into account. The light intensity including the effective finesse and this background noise is given by:

$$I_{\text{FP}}(r) = \frac{I_0}{1 + \left(\frac{2N_E}{\pi}\right)^2 \sin^2\left(\frac{\varphi}{2}\right)} + I_b \tag{21}$$

A non-linear least square minimization algorithm is performed in order to find the parameters Φ_0 and N_R, which will define the instrument function. The procedure minimizes the difference between the experimental interferogram and its theoretical counterpart, initially computed with guesses. The input parameters are the phase at the center Φ_0, the effective finesse N_E, and the incident and noise intensity I_0 and I_b, whose initial values are the maximum and minimum intensities. The first guesses of Φ_0 and order k are obtained by detecting the radii of the successive fringes r_N and using

Eq. (19) and (18) . Furthermore, the initial guess of N_E is determined using Equation (20).

The coordinates of the interferogram center (X_c, Y_c) are determined by binary filtering the interferogram and applying the Hough transform for circle detection. To minimise the error on the centre detection, several circles are considered, and the mean result is used. The image is then converted into a one-dimensional dataset: pixel intensity level as a function of radial distance from the centre. A routine is developed to increase the precision of the centre using the 1D dataset. The initial detection gives an interferogram with a certain FWHM. An error in the centre detection will broaden the rings and therefore the FWHM. Several centre position around the initial detection are tested, to find the smallest FWHM. The interferogram is then re-binned around this new centre position. The 1D data are then averaged over segments centered on reference rays r_i, of decreasing width with r_i, which amounts to averaging the intensity distribution over annular regions of the image of increasing average radius. The width of these rings depends on the average radius, so that the area covered by an annular region is identical from one region to another [12, 19]. The outer radius r_i of the i-th ring region is defined using the difference $\Delta = r_{i\max} - r_{i\max-1}$, refereed to as bin size, between the inner $r_{i\max-1}$ and outer radii $r_{i\max}$ of the last ring :

$$\begin{aligned} r_i &= \sqrt{i(2r_{i\max} - \Delta)\Delta} \\ r_i &= \sqrt{i} r_1 \end{aligned} \tag{22}$$

2. Rayleigh interferogram

The Rayleigh image is actually the convolution of the Rayleigh scattered light spectrum $S_R(x, y)$ and the instrument function $I_{\mathrm{FP}}(x, r)$ given by Eq (21) , determined in the first step. The instrument function was modelled for the laser incident light frequency, assuming a perfectly monochromatic light. Any phase change induced by a light wavelength different than that of the laser is measured as a relative change from that of the incident light. The frequency of the Rayleigh scattered light is expressed with the x parameter from Eq. (10). The phase is therefore due to wavelength difference, and is expressed as:

$$\varphi = \varphi_0 \left(1 - \frac{1}{2} \left(\frac{r}{f_f} \right)^2 + \frac{\lambda_0 u_0 \sqrt{2} x}{c \lambda_i} \right) \tag{23}$$

The instrument function is thus modelled for every frequency covered by the scattered light. In absence of any extraneous noise and light, the intensity of the Rayleigh scattered light on the camera is [1]:

$$I_{\mathrm{Rayleigh}}(r) = I_R \int_{-\infty}^{\infty} S_R(x, y) I_{\mathrm{FP}}(x, r) dx \tag{24}$$

where I_R is the intensity of the scattered light. The spectrum S_R defined as stated in Sec III.A.1 is computed using the Tenti S6 model. The code used is the MATLAB© transcription of the Pan *et al.* [20] FORTRAN© code. The modelled radial distribution of intensity is obtained by convoluting the spectrum and the instrument function, using Eq. (24). Using the optical setup of Figure 4, the Rayleigh image contains the laser beam modulated by the interferometer. Indeed without the interferometer, the laser beam would be observed in the image plane. The interferometer being on the optical path, it modulates the image according to the frequency content and the position of the source. That is why only circle arcs are observed. Only a part of this image is used, corresponding to the arcs of circle at their maximum intensity. This truncated image is converted into a one-dimensional dataset following the procedure described in the previous section. Then the temperature T and velocity u are found, as for the instrument function, with the non-linear least square minimisation *lsqnonlin* from MATLAB©.

IV. Test method

Evaluation of the precision of the interferogram processing routine is carried out on the basis of synthetic interferograms. These interferograms have been generated such that they have the same order of magnitude in annulus width, annulus radii, and SNR ratio as the experimental setup being currently developed at the laboratory. The interferograms being generated with known parameters, the error made while retrieving them from the image analysis can be assessed.

A. Synthetic interferogram generation

The relevant parameters of the optical setup simulated are the camera sensor resolution, 153,8 px/mm and the focal distance f_f =300 mm of the lens L_f. To simulate the integration effect on the camera pixel, images are generated with over discretization, typically 40 points per pixel, and are rasterized. Therefore, as the fringe width decreases from the center, the intensity of the maxima decreases with increasing r. The mirrors mounted in the interferometer provided by SLS Optics Ltd., have a reflectivity of 89% ± 1%. This corresponds to a factor $F = 294^{+66}_{-50}$ and a reflective finesse $N_R = 26^{+3,8}_{-1,5}$. The N_R chosen is thus 26. The mirrors are separated by spacers made of Ultra Low Expansion (ULE) glass by a distance $d = 20$ mm.

A laser beam shape function is determined to simulate the arc of circle of the Rayleigh interferogram. It has a unique peak level in the direction parallel to the beam and is a Gaussian in the direction perpendicular to the beam. It depends on the vertical origin h of the laser on the image and its FWHM σ. The angle θ is assumed to be close to zero. The Gaussian function is then given by :

$$L = 2\sqrt{2\pi}\sigma e^{\left(\frac{-(Y-h)^2}{2\sigma^2}\right)} \tag{25}$$

From the observation of the laser shape, σ is assumed to be $0{,}2.10^{-3}$ m. h is chosen so that the beam is at the image center, although the beam is on the median axis of the image or not depending on the optical adjustments that were made before the acquisition, and independently of the analysis that is made of this image a posteriori. Synthetic Rayleigh interferograms are generated corresponding to different flow conditions. The temperature and pressure conditions corresponds to those encountered in most experiments and thus fall into the kinetic regime. We simulate interferograms obtained under different flow conditions, at P=1 bar and T=293K . Under these thermodynamic conditions, the gas diffuses incident light according to the kinetic regime described in Sec III.A.1. Three flow velocities are considered here, 0., 260 and 261 m/s. Two high speed jets are considered with close velocities. This is done to ensure that small velocity variations can be detected. The room temperature T is arbitrarily chosen.

B. Parametric study

1. Interferometer transfer function characterisation

The main parameter of the procedure to obtain the 1D dataset from the 2D image is the value of the bin size Δ. A parametric study is performed to determine the optimal value of this parameter. From the same image, the procedure of transfer function determination described in Sec. III.C.1 is carried out with increasing values of Δ, expressed as a fraction of pixel. The values range from 0.05 to 1.4 times the pixel length. A second parameter of interest is the focal length f_f. Typically, manufacturers gives precisions of the order of the %, and focometry methods such as the Bessel method achieve the same order of precision. The procedure is then carried out with varying values of f_f as input parameters, from 290 to 310 mm, when the value used for the image generation is 300 mm.

Finally, during an acquisition, the value of Φ_0 is likely to be subject to a minor drift because of temperature variations. However, this variation does not induce a change of ring order because its relative magnitude with respect to 2π remains below 6% per degree of temperature change. Several interferograms are generated, with variations around an initial value from $\Phi_0 - \epsilon$ to $\Phi_0 + \epsilon$, where ϵ ranges from 0 to 3%×2π. Ultimately, this aims at assessing the precision of the determination of Φ_0.

For each iteration, the obtained finesse N_E and phase Φ_0 are compared to their original values. No noise is added to the synthetic interferograms at this step, since the signal to noise ratio (SNR) is expected to be really high (≈1500) in an experimental context.

2. Rayleigh interferogram characterisation

There are two main causes of error in the analysis of the Rayleigh interferogram. The first one would be an error in the determination of the interferometer transfer function. Roughly, a bias in the determination of the finesse would lead to an error in the temperature estimation, and an error in the determination of Φ_0 would lead to an error in the velocity estimation. Then a second cause of error would be the analysis of the Rayleigh image in itself. The quality of the image can be in cause, especially the SNR. In an experimental context, it is especially difficult to obtain a good SNR with non-intensified cameras capturing Rayleigh scattered light induced by 5W incident illumination and an image

without dust contamination. In the present experimental set-up, preliminary measurements shown that SNR of 3 can be expected. Moreover, the selection of a portion of the image, as stated in Sec. (IV.A), can induce a bias in the annular summing procedure. Indeed, as the the intensity is not homogeneous for one radius, the 1D dataset can be biased. The image portion taken into account is at the center of the interferogram, and has a 20 pixel height. Only one fringe is used here, to ensure a punctual probed volume (see Figure 1).

To assess the precision of the Rayleigh image treatment, interferograms are analysed with the prescribed, thus exact, transfer function, so that the only cause of error is induced by the Rayleigh interferogram processing in itself. This is done first from an analytical curve computed from Eq.(24), and then from the interferogram. This aim to asses the bias which can be caused by the annular summing and the image quality. The parametric study on the bin size will be carried out again, as less pixels are taken into account. This parametric study is made with the prescribed transfer function, and noisy images, since the advantage of the annular summing technique is to attenuate irregularities of the image. Several interferograms with added noise will be computed to establish a statistical estimation of the procedure's sensibility to the image noise. The generated noise is a random noise with a uniform distribution, and a set of 500 images is generated. The goal is to reproduce the camera sensor noise, at a SNR value of 3.

Finally, interferograms are processed with the transfer function from image analysis (Sec IV.B.1). These are the set of three interferograms corresponding to the flow conditions stated in the previous section. The comparison is made for one flow condition between the results obtained from the analytical curve of radial intensity distribution both with the prescribed and with the determined transfer function, and from the Rayleigh interferograms again with the known and determined transfer function.

V. Results

A. Reference interferogram analysis

The results of the optimal bin size Δ determination are now reported. The finesse determination is shown in Figure 6a. The better fit is obtained for $\Delta = 0.1$ pixel length. For smaller values, the 1D dataset is over sampled and the procedure fails to give a reasonable estimation, up to 50% of error to the expected value. For larger values of Δ around 1 px, the relative error increases up to 20%. Figure 6b shows the results on the reference phase Φ_0. Except when the data are over sampled, no clear variation of Φ_0 are observed and the relative error to the expected value is well under 1%. Finally, the evolution of the total relative error is shown in Figure 6c. The total error follows the evolution of the error on the finesse, and increases up to 20%. Therefore, the optimal value of Δ for determining the transfer function of the interferometer is 0.1 pixel length. All the following transfer function are computed using this value.

The results of the procedure with a change in the value for f_f are represented in Figure 7. As shown by the two first Figures 7a and 7b, this has a low impact on the fitting procedure outcome. The relative errors on Φ_0 and N_E due to any uncertainty in the value of f_f within ±3% do not exceed 0.85% for N_E and 8, 10^{-4}% for Φ_0. As a consequence, the total error plotted in Figure 7c stays under 1% within the tested range.

Figure 8 shows the determined parameters for varying Φ_0. As observed in Figure 8a, for every initial values of Φ_0, the procedure succeeds to give a proper estimation of the finesse with a relative error smaller than 1%. The results on the phase, shown in Figure 8b indicate that the algorithm is able to detect small variation of Φ_0. For every initial value, the committed error is less than 0,01%. Then, as the error committed on the finesse is the dominant, the total relative error plotted in Figure 8c follows its variations, and stays within 1%. The transfer function determination is to be made with a bin size $\Delta = 0, 1$ pixel length. Using this value, the algorithm succeed to give an estimation of the finesse N_E with a precision superior to 99% however, it is always slightly underestimated. This precision is achieved for either imprecise values of f_f, or for several initial values of Φ_0. The influence of this small bias on the temperature estimation is highlighted in the following section. The determination of Φ_0 is less prone to error, as for varying values of f_f and initial values of Φ_0, it shows error of less than 0.01%. This being the only cause of bias, it would leads to an error of less than 0.1 m/s for the estimation of u.

B. Rayleigh interferogram analysis

The optimal bin size value is determined for the Rayleigh interferograms on the central image portion. Results are shown in Figure 9. Figure 9a displays the results on the fitted temperature T. The error is maximum for small values of Δ. It decreases as Δ increases up to a plateau where it oscillates between -1 and 1 %. Figure 9b shows the results on velocity estimations. The tendency is the same as for the temperature, while the error committed is lesser than 1%

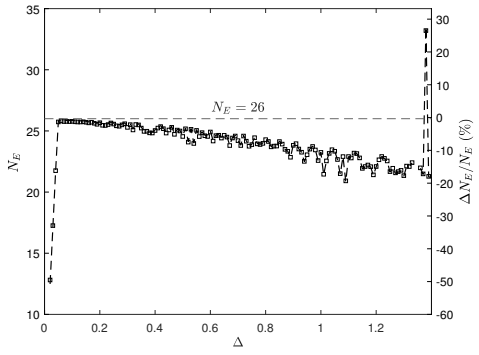

(a) □: Determined finesse; - -: Relative error

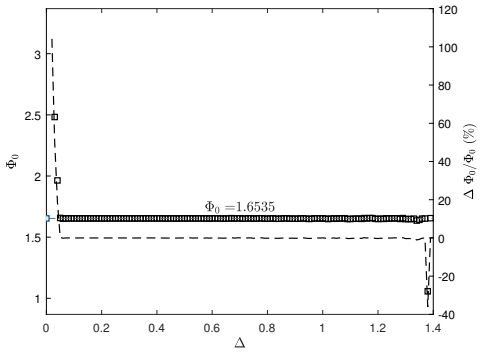

(b) □: Determined Φ_0; - -: Relative error

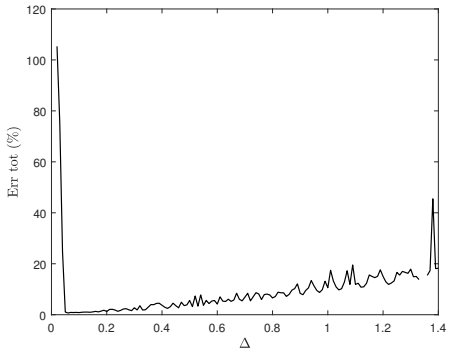

(c) Total relative error

Fig. 6 Fitted parameters of the interferogram transfer function for varying bin size and their relative error

for all values of Δ. Finally, the total error is plotted in Figure 9c. For Δ between 0,6 and 1,8 pixel length (maximum tested here), the total error on T and u (calculated with $e = \sqrt{(\Delta u/u)^2 + (\Delta T/T)^2}$) does not exceed 1%. Therefore, the following analyses are performed with Δ=0,8.

Table 1 displays the results of the procedure applied to three flow conditions. The procedure is carried out first from the analytical curve from Eq. (24) and then from the interferogram. Each is also computed with the already known transfer function, and the determined transfer function. As expected, the procedure is more precise in using the analytical curve. With the known transfer function, the flow features are perfectly retrieved. Using the determined transfer function, the error on the velocity is less that 0,1 m/s and the error on the temperature is of the order of 0,5 K. The image treatment induces a small bias in the flow parameters estimation. Indeed, with the known transfer function, the error on the velocity is up to 0,5 m/s and 0,4 K for the temperature. Using the determined transfer function the error on the temperature is of the same order, 0,6 K at maximum and no clear difference is observed for the velocity. Note that both the velocity and temperature are slightly underestimated in each case.

Transfer function		u amb (m/s)	T amb (K)	u jet (m/s)	T jet (K)	u jet$_2$ (m/s)	T jet$_2$ (K)
Analytical curve	Known	0	293	260	293	261	293
	Identified	$-1{,}25.10^{-2}$	292,4	259,9	292,5	260,9	292,5
Interferogram	Known	-0,31	293,04	259,5	292,6	260,57	292,68
	Identified	-0,41	292,5	259,69	292,4	260,69	292,44

Table 1 Results of the fitting procedure from analytical curve and image processing for three flow conditions

The error committed on the fitting procedure when noise is present on the image is assessed. The procedure is carried out with the known transfer function so that there is no other cause of error than the image treatment and the

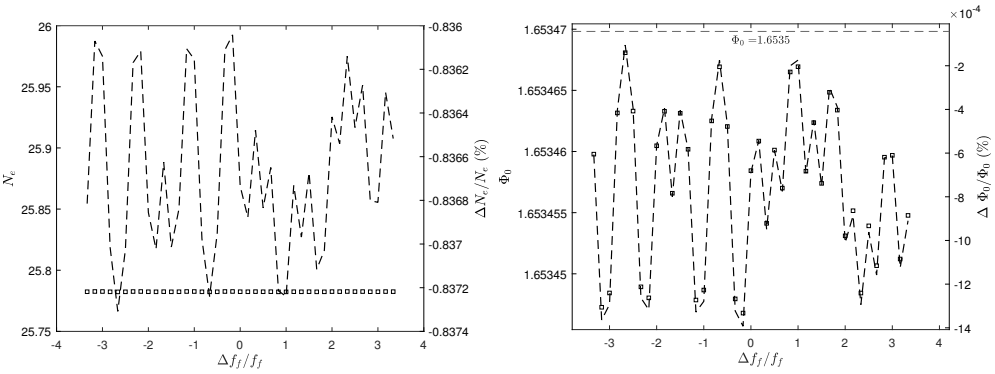

(a) □: Determined finesse; - -: Relative error **(b) □: Determined Φ_0; - -: Relative error**

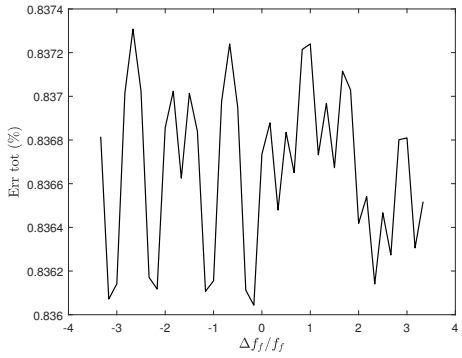

(c) Total relative error

Fig. 7 Fitted parameters of the interferogram transfer function for varying focal length f_f and their relative error

quality of the image. Results are shown in Figure 10. It displays histogram of the relative error on the temperature, velocity and the total relative error, for 500 interferograms with random noise. There is a Gaussian distribution of error on the temperature, centred between -2 and -1 %. The error on the velocity is centred on 0 %, even though there is a slight tendency to the underestimation of the velocity, up to -1 %. Figure 10c highlights the fact that the interferograms are processed with enough precision so that the total error does not exceed 2% for the 4/5 of the interferograms.

VI. Conclusion

A post processing routine has been developed for the analysis of Fabry-Pérot interferograms. This aimed to analyse the signal from Rayleigh scattering applied to a free flow. These interferograms were analysed with a least-square minimization, and the transfer function of the aforementioned interferometer. The precision of the post processing routine was assessed from synthetics interferograms, for both the instrument transfer function and Rayleigh scattered light. This first allowed to establish a baseline of the maximum achievable precision for the interferometer transfer function, which is less than 1% error for the finesse and of the order of 0.01% error for the phase. Then, flow velocity and temperature were estimated from synthetic Rayleigh interferograms, using the already known and determined transfer function of the instrument. For both case the procedure succeed to give proper estimations, with precision up to 0.5 K and 0.4 m/s. Random noise was added to the Rayleigh interferogram to simulate experimental interferograms and assess the robustness of the routine. It was assessed on numerous interferograms, and the total relative error does not exceeded 4%. The procedure will be used on experimental interferogram to asses the experimental error.

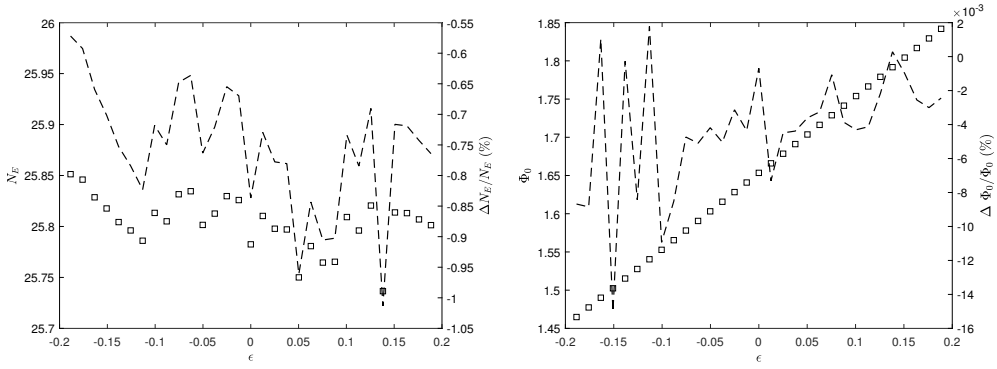

(a) □: Determined finesse; - -: Relative error **(b) □: Determined Φ_0; - -: Relative error**

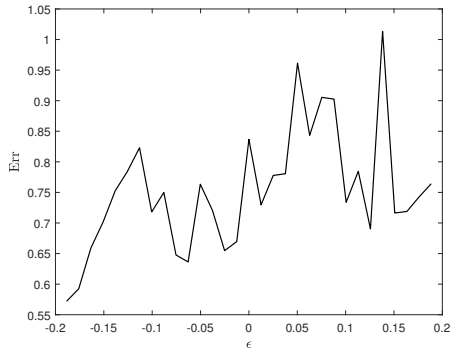

(c) Total relative error

Fig. 8 Fitted parameters of the interferogram transfer function for varying Φ_0 and their relative error

Acknowledgements

This work was performed within the framework of the industrial chair ARENA (ANR-18-CHIN-0004-01) co-financed by Safran Aircraft Engines and the French National Research Agency (ANR), and in the framework of the Labex CeLyA (ANR-10-LABX-0060) of the Université de Lyon, within the program "Investissements d'Avenir" (ANR-16-IDEX-0005) operated by the French National Research Agency (ANR).

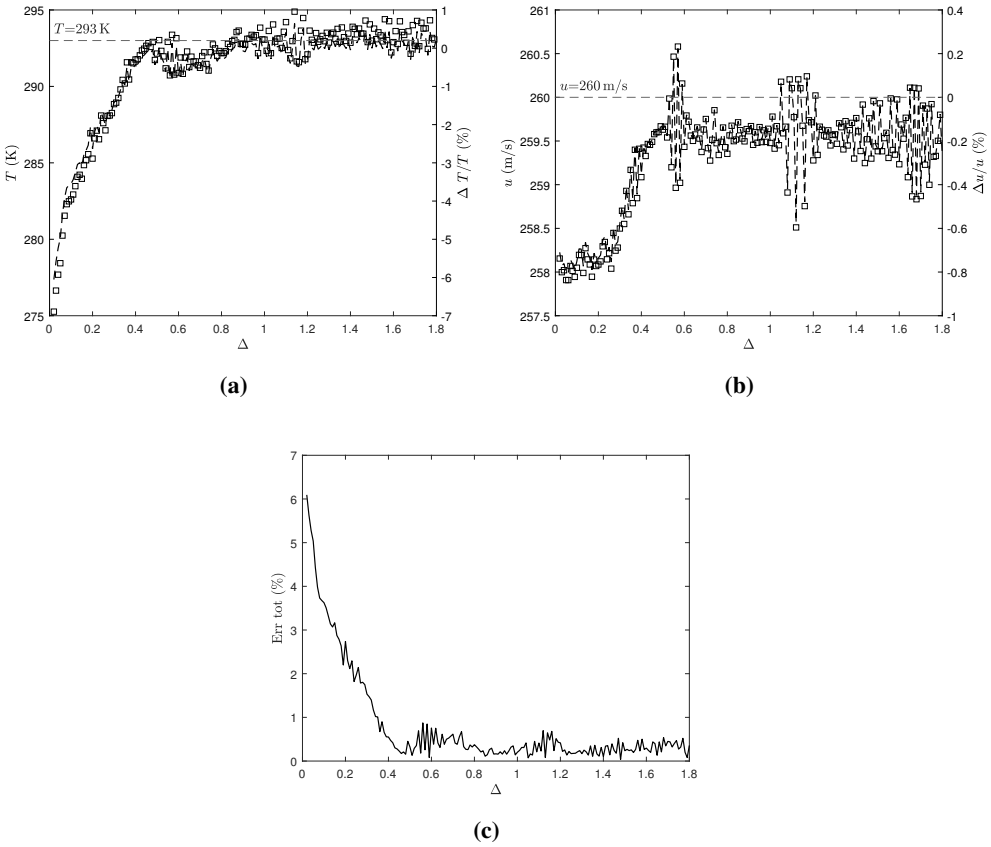

Fig. 9 Fitted parameters of the Rayleigh interferogram for varying bin size and their relative error

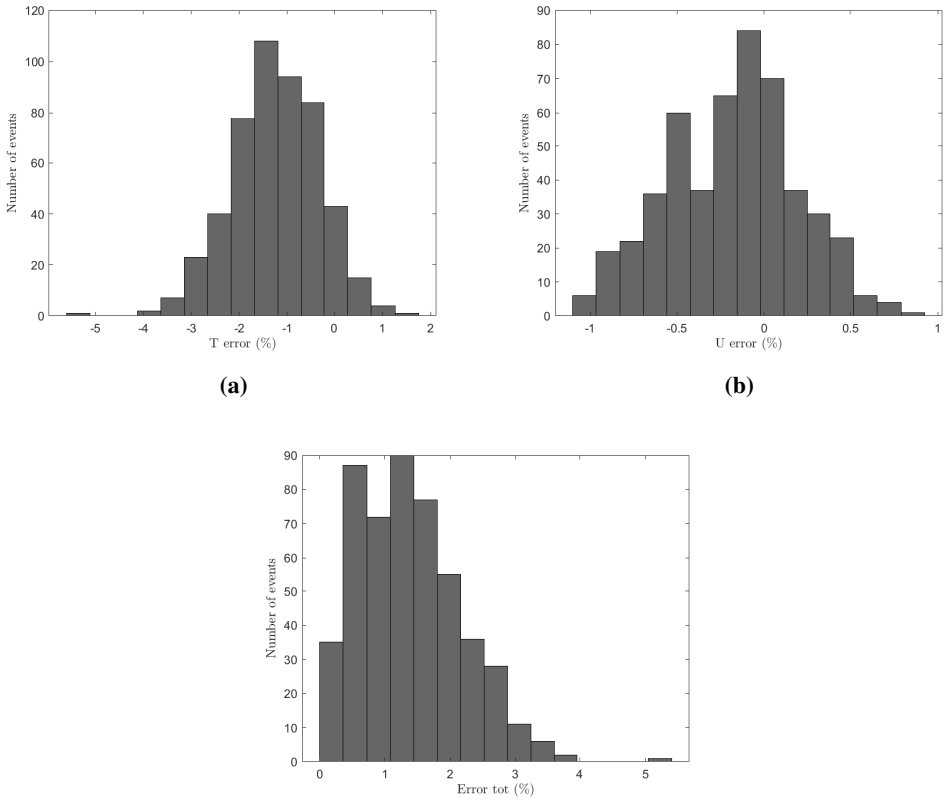

(a) **(b)** **(c)**

Fig. 10 Histograms of the relative error on T, U and total relative error for noisy data.

References

[1] Panda, J., "Spectrally-resolved Rayleigh scattering to measure velocity, temperature, density, and density fluctuations in high-speed flows," *Exp. Fluids*, Vol. 61, No. 3, 2020, pp. 1–16. https://doi.org/10.1007/s00348-020-2903-2, URL https://doi.org/10.1007/s00348-020-2903-2.

[2] Mielke, A. F., "Development of a Molecular Rayleigh Scattering Diagnostic for Simultaneous Time-Resolved Measurement of Temperature, Velocity, and Density," 2008, p. 185.

[3] Panda, J., and Seasholtz, R., "Velocity and temperature measurement in supersonic free jets using spectrally resolved Rayleigh scattering," *37th Aerosp. Sci. Meet. Exhib.*, American Institute of Aeronautics and Astronautics, Reston, Virigina, 1999, pp. AIAA 99–0296. https://doi.org/10.2514/6.1999-296, URL http://arc.aiaa.org/doi/10.2514/6.1999-296.

[4] Mercier, B., Castelain, T., Jondeau, E., and Bailly, C., "Density fluctuations measurement by rayleigh scattering using a single photomultiplier," *AIAA J.*, Vol. 56, No. 4, 2018, pp. 1310–1316. https://doi.org/10.2514/1.J056507.

[5] Fagan, A. F., Clem, M. M., and Elam, K. A., "Improvement in rayleigh scattering measurement accuracy," *50th AIAA Aerosp. Sci. Meet. Incl. New Horizons Forum Aerosp. Expo.*, , No. January, 2012. https://doi.org/10.2514/6.2012-1060.

[6] Chen, L., Yang, F. R., Su, T., Bao, W. Y., Yan, B., Chen, S., and Li, R. B., "High sampling-rate measurement of turbulence velocity fluctuations in Mach 1.8 Laval jet using interferometric Rayleigh scattering," *Chinese Phys. B*, Vol. 26, No. 2, 2017. https://doi.org/10.1088/1674-1056/26/2/025205.

[7] Cutler, A. D., Rein, K., Roy, S., Danehy, P. M., and Jiang, N., "100-kHz Interferometric Rayleigh Scattering for multi-parameter flow measurements," *Opt. Express*, Vol. 28, No. 3, 2020, p. 3025. https://doi.org/10.1364/oe.380934.

[8] Estevadeordal, J., Jiang, N., Cutler, A. D., Felver, J. J., Slipchenko, M. N., Danehy, P. M., Gord, J. R., and Roy, S., "High-repetition-rate interferometric rayleigh scattering for flow-velocity measurements," *Appl. Phys. B Lasers Opt.*, Vol. 124, No. 3, 2018, pp. 1–6. https://doi.org/10.1007/s00340-018-6908-y, URL http://dx.doi.org/10.1007/s00340-018-6908-y.

[9] Bivolaru, D., Cutler, A., and Danehy, P., "Spatially- and Temporally-resolved Multi-parameter Interferometric Rayleigh Scattering," 2011, pp. 1–10. https://doi.org/10.2514/6.2011-1293.

[10] Mercier, B., Jondeau, E., Castelain, T., Ozawa, Y., Bailly, C., and Comte-Bellot, G., "High frequency temperature fluctuation measurements by Rayleigh scattering and constant-voltage cold-wire techniques," *Exp. Fluids*, Vol. 60, No. 7, 2019. https://doi.org/10.1007/s00348-019-2753-y, URL https://doi.org/10.1007/s00348-019-2753-y.

[11] Seasholtz, R. G., Buggele, A. E., and Reeder, M. F., "Flow measurements based on Rayleigh scattering and Fabry-Perot interferometer," *Opt. Lasers Eng.*, Vol. 27, No. 6, 1997, pp. 543–570. https://doi.org/10.1016/S0143-8166(96)00063-2.

[12] Coakley, M. M., Roesler, F. L., Reynolds, R. J., and Nossal, S., "Fabry–Perot CCD annular-summing spectroscopy: study and implementation for aeronomy applications," *Appl. Opt.*, Vol. 35, No. 33, 1996, p. 6479. https://doi.org/10.1364/ao.35.006479.

[13] Miles, R. B., Lempert, W. R., and Forkey, J. N., "Laser Rayleigh scattering," *Meas. Sci. Technol.*, Vol. 12, No. 5, 2001. https://doi.org/10.1088/0957-0233/12/5/201.

[14] Tenti, G., Boley, C. D., and Desai, R. C., "On the Kinetic Model Description of Rayleigh–Brillouin Scattering from Molecular Gases," *Can. J. Phys.*, Vol. 52, No. 4, 1974, pp. 285–290. https://doi.org/10.1139/p74-041, URL http://www.nrcresearchpress.com/doi/10.1139/p74-041.

[15] Gu, Z., Witschas, B., van de Water, W., and Ubachs, W., "Rayleigh–Brillouin scattering profiles of air at different temperatures and pressures," *Appl. Opt.*, Vol. 52, No. 19, 2013, p. 4640. https://doi.org/10.1364/AO.52.004640, URL https://www.osapublishing.org/abstract.cfm?URI=ao-52-19-4640.

[16] Mielke, A. F., Elam, K. A., and Sung, C.-J., "Rayleigh scattering diagnostic for measurement of velocity and density fluctuation spectra," *40th AIAA Aerosp. Sci. Meet. Exhib.*, , No. January 2006, 2006, pp. 1–15. https://doi.org/10.2514/6.2002-827.

[17] Mielke, A. F., Seasholtz, R. G., Elam, K. A., and Panda, J., "Time-average measurement of velocity, density, temperature, and turbulence velocity fluctuations using Rayleigh and Mie scattering," *Exp. Fluids*, Vol. 39, No. 2, 2005, pp. 441–454. https://doi.org/10.1007/s00348-005-0990-8, URL http://link.springer.com/10.1007/s00348-005-0990-8.

[18] Vaughan, J. M., *The Fabry–Perot Interferometer*, Routledge, 2017. https://doi.org/10.1201/9780203736715, URL https://www.taylorfrancis.com/books/9781351410519.

[19] Makela, J. J., Meriwether, J. W., Huang, Y., and Sherwood, P. J., "Simulation and analysis of a multi-order imaging Fabry-Perot interferometer for the study of thermospheric winds and temperatures," *Appl. Opt.*, Vol. 50, No. 22, 2011, pp. 4403–4416. https://doi.org/10.1364/AO.50.004403.

[20] Pan, X., Shneider, M. N., and Miles, R. B., "Coherent Rayleigh-Brillouin Scattering," *Phys. Rev. Lett.*, Vol. 89, No. 18, 2002, pp. 1–4. https://doi.org/10.1103/PhysRevLett.89.183001.